OVERVIEW OF THE NUMERICAL SIMULATIONS OF A HIGH-LIFT-DEVICE NOISE MEASUREMENT MODEL

Taro IMAMURA *, Hiroki URA *, Yuzuru YOKOKAWA*,
Kentaro TANAKA, Tohru HIRAI**, and, Kazuomi YAMAMOTO***

***Japan Aerospace Exploration Agency, ** Ryoyu Systems Ltd. Co.**

Keywords: *Airframe Noise, High-lift-device, Computational Fluid Dynamics*

Abstract

Overview of the computational fluid dynamics (CFD) research activities, associated with a simplified high-lift-device wind tunnel model (OTOMO) is described. Three different CFD codes are used to investigate the flow around the OTOMO focusing on different aspects. First, two different codes, UPACS (structured grid) and TAS (unstructured grid), codes are used to estimate the aerodynamic performance. Secondly, unsteady flow simulation is performed to understand the noise generation mechanism around OTOMO, specially, slat noise. For this purpose, UPACS-LES code is used. Validation of the computational results is performed through comparison with the experimental results. And finally, noise reduction devices are designed and evaluated with the support of CFD. All of the computations are performed parallel to the wind tunnel experiments, which led the overall program successful.

1 Introduction

Airframe elements are a dominant noise source during a landing phase of a civil aircraft due to the decrease in jet engine noise. Nearly 50% of the overall noise during the landing phase is generated by the airframe structures such as slats, flap edges of high-lift-devices (HLD), and landing gears [1-2]. To further lower the overall noise level, reduction of the airframe noise is necessary.

From the previous studies, slat and flap-tip are recognized as a dominant airframe noise sources. The first attempt in JAXA was noise source measurement using phased-array microphone, during the aerodynamic testing of a realistic high-lift configuration aircraft model (JSM: JAXA High-Lift configuration Standard Model) [3-5] in a low speed wind tunnel (See Fig. 1). The necessity of further research on this topic as well as importance of HLD noise was recognized from the results.

Figure 1. JAXA High-lift configuration standard model in 6.5 x 5.5 m wind tunnel (JAXA-LWT1).

In order to investigate details of HLD noise, a simplified high-lift wing model, called OTOMO [6,7], was designed based on the airfoil section of the JSM. The model was decided to be a half-span type as shown in Fig. 2 to maximize Reynolds number. The chord length is 0.6m, the half wing span is 1.35m, and the aspect ratio is 4.5. For the simplification, sweep angle, taper and dihedral angle were omitted. The model consists of full-span slat at the leading-edge and 70% span single-slotted flap at the T.E. In addition, it is equipped with a simplified body-pod of 1.65m in length, 0.4m in

width, and 0.05m in height formed by elliptic cross sections. It is possible to use this model in four kinds of HLD configurations by deploying or stowing the slat and/or the flap. The model was designed for the purpose of measuring noise from a HLD, mainly from slat, slat supports and flap edge. Another important point was to test variable noise reduction concepts from both aerodynamic and acoustic points of view. To concentrate on these items, the wing is designed as simple as possible. The previous works are summarized by Yokokawa *et al.* [6] and Ura *et al.* [7].

Figure 2. Simplified HLD model in 2.0 x 2.0m wind tunnel (JAXA-LWT2).

This paper summarizes the computational fluid dynamics (CFD) research activities, associated with this wind tunnel experiment. Three different CFD codes are used depending on the complexity of the computational model and flow physics to focus on. Validation of the computational results is performed through the comparison with the experimental results. Subsequently, computational results are used to understand the detail flow physics around the HLD, which is difficult to gain information in the wind tunnel experiment.

This paper is organized as follows. In Section 2, the flow solvers that are used in this study are briefly described. In Section 3, the baseline characteristics of OTOMO are investigated. In Section 4, several noise reduction concepts for slat will be presented. Finally, Section 5 concludes this paper.

2 Flow Solvers, Meshes, and Flow Conditions

Three different kind of flow solvers are used to investigate the flow field around the simplified high-lift configuration model.

The first code is the UPACS-1.4 (Unified Platform for Aerospace Computational Simulation version 1.4) code [8-10], which is a standard CFD code in JAXA. This code solves Reynolds-averaged Navier-Stokes (RANS) equation based on a cell-centered finite-volume method on multi-block structured grids.

The second code is the TAS (Tohoku University Aerodynamic Simulation) code [11-13]. In TAS_Flow, RANS equations are solved on the unstructured mesh by a cell-vertex finite volume method. MEGG3D is an unstructured mesh generator with graphical user interface (GUI) tools [14-17]. It can generate triangular surface mesh with the advancing front method and tetrahedral volume mesh using Delaunay tetrahedral meshing, as well as hybrid volume mesh composed of tetrahedrons, prisms, and pyramids for viscous flows with high Reynolds number.

The third code is the UPACS-LES code [18-20]. The governing equations are favre-filtered compressible Navier-Stokes equations for large-eddy-simulations (LES). The basic frame of this program is almost consistent with the UPACS-1.4 code described above. To calculate the generation and advection of vortices and propagation of acoustic waves with relatively small number of grid points, higher-order scheme is used in the simulations (6th-order compact scheme developed by Kobayashi [21]).

Table 1. Details of CFD codes

	UPACS-1.4	TAS	UPACS-LES
Mesh	Structured	Unstructured	Structured
Flow	Steady	Steady	Unsteady
Governing Eq.	RANS*1	RANS*1	LES*2
Turbulence Model	Spalart-Allmaras one Eq.	Spalart-Allmaras one Eq.	Standard Smagorinsky (Cs=0.1)
Time Int.	MFGS*3	LU-SGS*4	MFGS*3 (5 sub. ltr.)
Convection	Roe scheme (3rd order)	HLLEW*5 method	6th order compact scheme
Viscous	2nd order	2nd order	2nd order

*1 Reynolds Averaged Navier-Stokes
*2 Large Eddy Simulation
*3 Matrix Free Gauss-Seidel implicit method
*4 Lower/Upper Symmetric Gauss-Seidel
*5 Harten-Lax-vanLeer-Einfeldt-Wada

The details of each flow solvers are summarized in Table 1. All of the flow conditions presented in this paper correspond to the mean flow velocity of 60m/s for a wind tunnel scale (the reference length is the chord length of OTOMO, which is 0.6m).

3 Baseline Characteristics

3.1 Steady-state Flow

First of all, three dimensional steady-state flow fields are calculated to investigate the basic aerodynamic characteristics, such as lift and drag of the baseline configuration. Additionally, steady-state flow patterns, such as spanwise effect due to the downwash from the wing tip vortex, and flow patterns which is relevant to noise generation, are focused. For the purpose described above, 3D computations using UPACS-1.4 and TAS are performed.

The model configuration is approach condition (slat and flap deployed). The brackets to support the high-lift devices were removed in the computations. Figures 3 & 4 show the meshes used in the calculations. The structured mesh for UPACS-1.4 consists of about 20 million cells and that of TAS is around 6 million. The minimum spacing for both meshes in the normal direction to the wing surface are $0.01/\sqrt{\ }$ Re.

Figure 5 shows the C_L-α curves from the computations and are compared with the experimental results. Although the flow solvers and the mesh size used in the computations are different, qualitative agreement is observed up to 16 degrees. However, if we compare the results in detail, the difference in C_L at AoA of 8 degrees is about 0.05, which corresponds to approximately 3% of the C_L at that AoA. Based on the discussions by Murayama *et al.* [22], 1 to 2% difference could be observed when comparing the results with and without laminar separation at the leading edge. Also, slat and flap supports, which were not included in the computation, will decrease the lift by few percentages. These points should be investigated for further comparison between the experiment and computations.

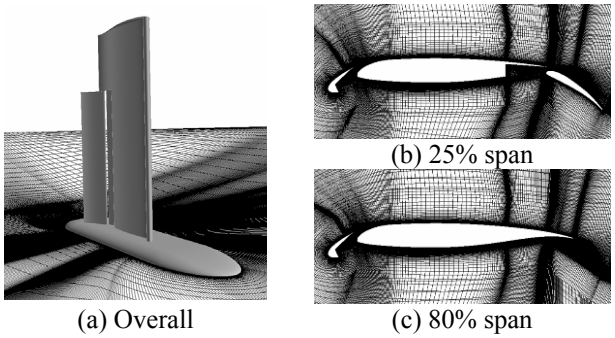

Figure 3. Structured mesh for UPACS-1.4 code

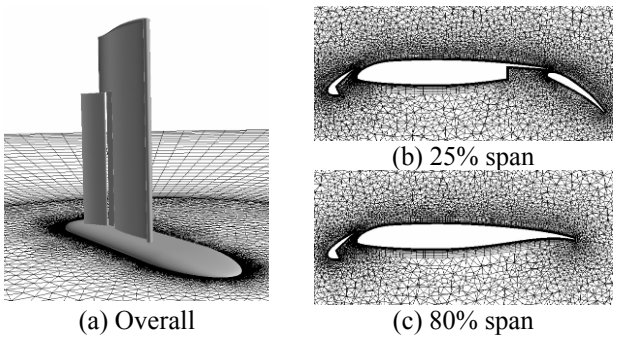

Figure 4. Unstructured mesh for TAS code

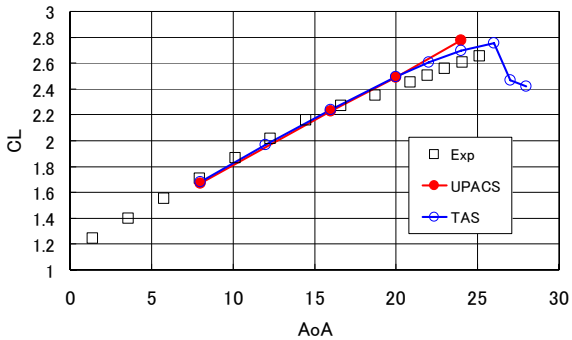

Figure 5. C_L-α curve for OTOMO configuration

Next, surface pressure coefficient (C_p) distributions are shown in Fig. 6, 7 and 8. The locations of the cross sections where pressure

taps are located are shown in Fig. 6. At 25% and 80% spanwise locations, the wing elements are three and two, respectively. The results are compared with the wind tunnel data. Both UPACS-1.4 and TAS show qualitative agreement with the experimental results at both cross sections. However, the height of the negative suction peaks on each wing elements does not show similar tendency. For example, CFD results becomes higher compared with the experiment at the peaks on the slat, but this is opposite on the main element. One possibility is the wind tunnel wall effect on the model. The computation assumes free flight condition, but the experimental model is inside the hard wall wind tunnel. Although, lift coefficients could be corrected based on the analytical method and effective AoA could be given, it is difficult to correct the local effective AoA through out the whole span. One solution to this problem is use a wind tunnel which has a larger cross section.

At 69% spanwise location, the C_p distribution is quite different between UPACS-1.4 and TAS as shown in Fig. 8. High negative suction peak around x/c=2.18 in the experimental result indicates an existence of strong longitudinal vortex at the upper side of the flap-tip region. This vortex is realized as a cause of the flap-tip noise. This peak was captured by the UPACS-1.4, but it became lower in TAS result. Since the mesh sizes used in the computations are different between the two computations, it is not fair to say that UPACS-1.4 is better flow solver. But, in general, capturing vortical phenomenon using unstructured mesh is much more difficult due to the numerical dissipations [23].

In order to compare the results in more direct manner, the TAS results are interpolated to the structured grid used for UPACS-1.4 computation and is subtracted from the UPACS-1.4 results. Figure 9 shows the difference in C_p (UPACS result minus TAS results). The isosurface in red indicates the region which UPACS-1.4 results are higher by 0.1 in C_p, and the blue region is the opposite. It is clearly observed that the difference appears around the wing-tip, flap-tip and wing-body interface. These indicate that more dense mesh is necessary in these regions, especially for TAS simulation. Further investigations on mesh dependency are also necessary for UPACS-1.4. It is important to clarify the effect of the spatial mesh resolutions to the aerodynamic performance.

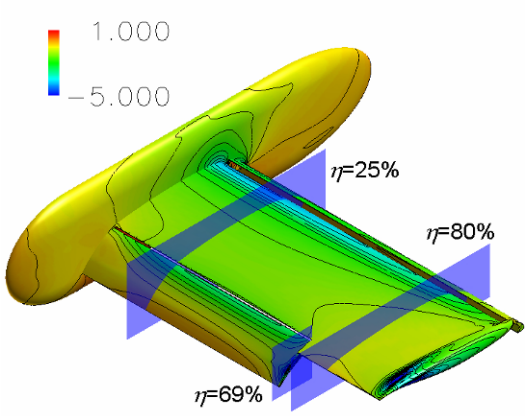

Figure 6. Surface Cp distribution at α=16deg (UPACS)

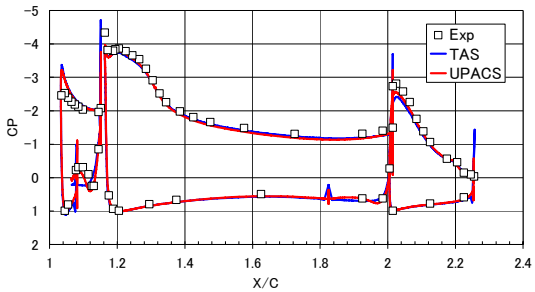

(a) 25% span cross sectional plane

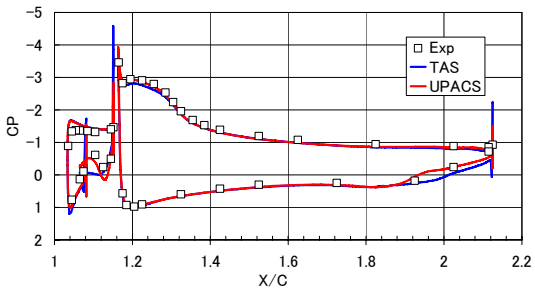

(b) 80% span cross sectional plane

Figure 7. Comparison of surface Cp distribution (UPACS-1.4 & TAS : 16 degrees, Experiment : Geometric AoA of 12 degrees) .

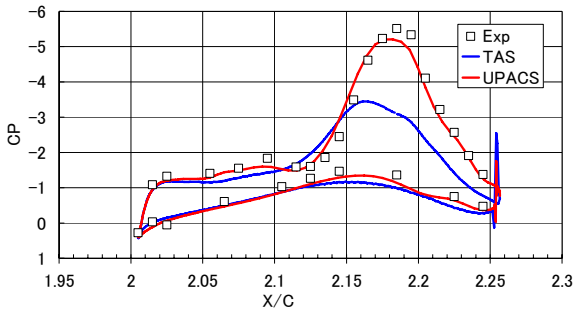

Figure 8. Comparison of surface Cp distribution at η=69% span location (UPACS-1.4 & TAS : 16 degrees, Experiment : Geometric AoA of 12 degrees) .

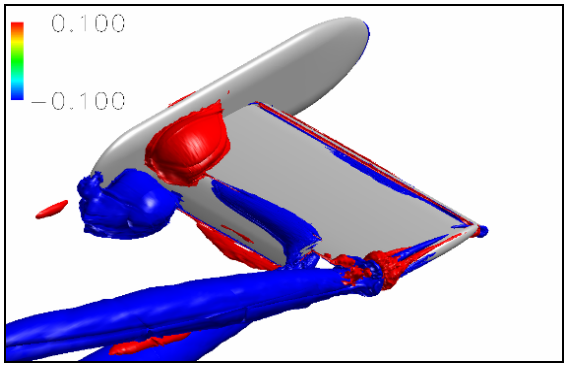

Figure 9. Difference in spatial C_p distribution between UPACS and TAS. (AoA=16 degrees)

It should be added that mesh generation effort is significantly different between these two flow solvers. The mesh generation for the structured mesh is approximately 1 month by an expert, while that of the unstructured mesh was about 1 day. Therefore, suitable flow solvers have to be chosen depending on the problem. If detail information of the vortical flow structures is necessary for only one (or two) geometries and changing flow conditions as a parameter, UPACS-1.4 is better. On the other hand, if multiple geometries have to be investigated, TAS will be better choice under the limitation of accuracy. Additional example will be shown in Section 4.

3.2 Unsteady-state Flow.

Unsteady flow computation is essential for understanding the noise generation mechanism, but full 3D computation around HLD is still difficult study to be done.

In this study, three-dimensional unsteady computation for the slat is performed using UPACS-LES code. The size of the LES computational domain is reduced by applying following methods. The computational domain in spanwise domain is limited to 33.3% of the slat chord and periodic boundary condition is applied as shown in Fig. 10 based on the previous study [18]. Additionally, zonal LES/RANS hybrid method is used to limit LES computation only around the slat regions (The rest of the region is solved by RANS). The overall mesh points are approximately 8 million points.

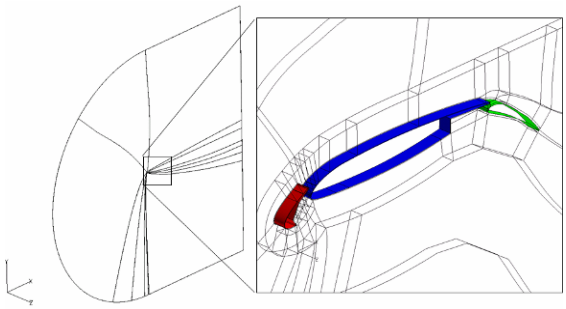

Figure 10. Computational grid for UPACS-LES simulation

The turbulence structures are exhibited by showing a positive iso-surface of the second invariant of the velocity gradient tensor Q.

$$Q = \frac{1}{2}\left(\Omega_{ij}\Omega_{ij} - S_{ij}S_{ij}\right) = -\frac{1}{2}\frac{\partial u_i}{\partial x_j}\frac{\partial u_j}{\partial x_i} > 0 \qquad (1)$$

From this result, locations of the vortex tubes regions are visualized. Figure 11 shows the isosurface of Q =500 at AOA of 4 and 8 degrees. The vortical flow structures can be classified into 5 regions. The first region is in the mixing layer near the cusp, where vortical structures in spanwise direction are observed. The second region is along the shear layer from the cusp. The spanwise vortices break into smaller fragments and impinge on the lower surface of the slat. The third region is the recirculation region inside the slat cove. The distribution of relatively weak vortices is observed inside this

region. The forth is the downstream region of the reattachment point of the shear layer. Here, longitudinal vortices are observed [18]. These vortices streams to the T.E. of the slat. Finally, the fifth is observed in the wake of the T.E. The vortex shedding caused by the thickness of the T.E. is observed. These features are the same for both AoA, but the strength of each region differs. For example, the shear layer from the cusp tends to become weaker as AoA increases. Also, the reattachment point on the lower surface moves to the upstream direction. These features are consistent with the PIV measurement data [6].

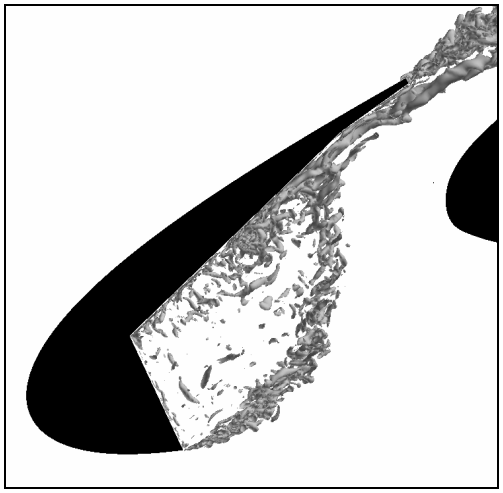

(a) AoA=4deg

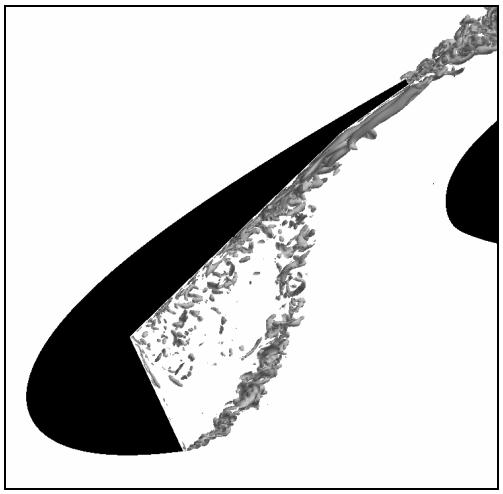

(a) AoA=8deg

Figure 11. Instantaneous iso-surface of the second invariant of the velocity gradient tensor.

Figure 12 shows the power spectral density (PSD) of C_p around the slat cove region. The calculated points correspond to the points where the unsteady pressure taps are located in the experimental model. The LES/RANS simulation of 8 degrees is compared with the experimental results at 8, 14, and 20 degrees. At these three locations (point A, B and C), good agreement with the experimental data is observed, excluding relatively high peak which is only observed in the computation. It is estimated at this point that larger PSD level of this peak compared with the experiment is due to numerical error caused around the block boundary and further improvements will be performed in the near future.

4 Evaluations of Noise Reduction Devices

As described in the previous section, the shear layer generated from the slat cusp is estimated to be responsible for the noise generation of low frequency broadband noise around a slat. Therefore, one of idea to reduce slat noise is to eliminate the shear layer from the cusp. Moreover, it is important to maintain the aerodynamic performance of the wing, since it is the main purpose of HLD.

Two different types of devices are introduces here as shown in Fig. 13. The first device is a slat cove filler (SCF). SCF is a device which fills up the cove region of the baseline slat to eliminate the separation from the slat cusp. There are several ways to design this device. This paper will focus on SCF2D, which is designed based on the dynamic pressure field of the baseline configuration (AoA is 2 degrees). Another device is called a thin slat (TS). The cusp region is shaved off from its baseline configuration, but its leading edge radius is maintained and smoothly connected to the trailing edge of the slat. The device shown in Fig. 13 is called TSF, because the lower surface of the thin slat is formed by a straight line from the leading edge circle to the trailing edge. In some ways, this slat could be understood as an independent small wing at the leading edge. The details are described in Imamura *et al.* [24].

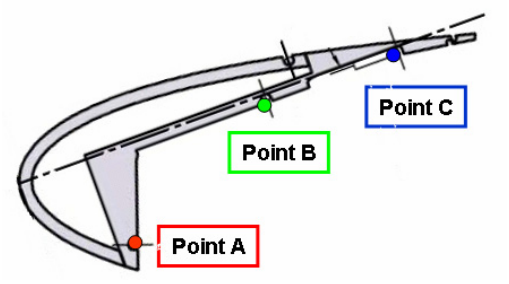

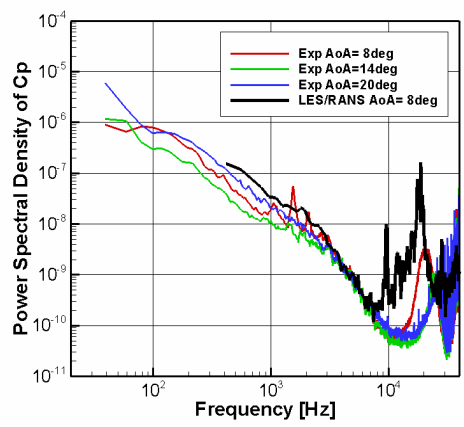

(a) Point A

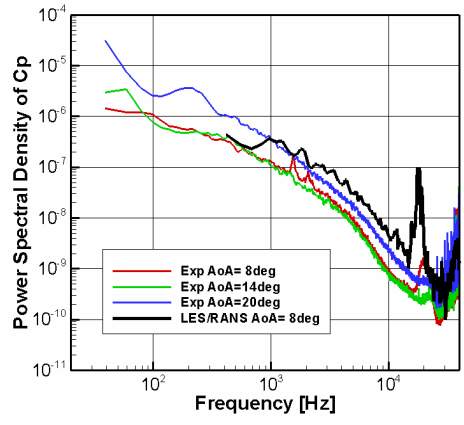

(b) Point B

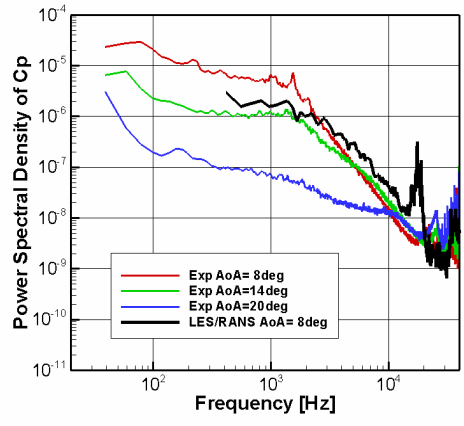

(c) Point C

Figure 12. Comparison of PSD of Cp around the slat (UPACS-LES, AoA=8degrees)

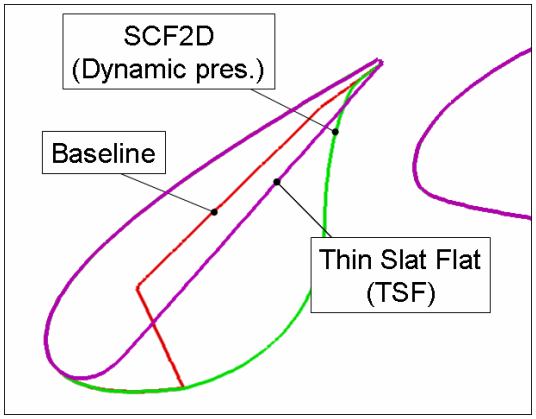

Figure 13. Low noise slat geometries (SCF2D and TSF)

Firstly, 2D computations were performed using UPACS-1.4 code. The flow conditions are freestream velocity of 60 m/s and AoA of 2 degrees, which is a design AoA for the SCFs. Figure 14 shows the Mach number distributions around slat regions for all cases. At this flow condition, flow around the lower surface of the slat region is mostly attached without separated flow for both airfoils. Figure 15 shows the C_l-α curve in 2D. Although the geometry changes significantly, the lift performance is almost consistent with the baseline configuration.

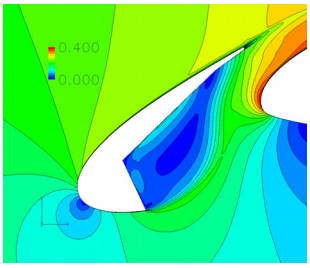

(a) Baseline

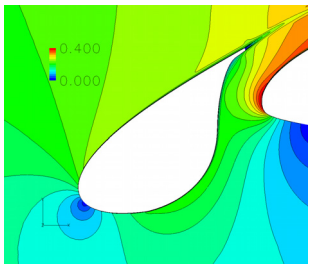

(b) SCF2D

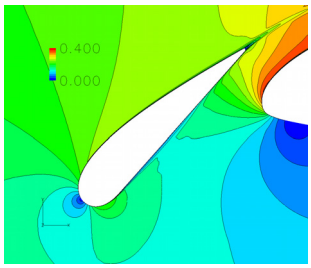

(c) TSF

Figure 14. Mach number distribution around baseline, SCF2D, and TSF (2D simulation using UPACS-1.4)

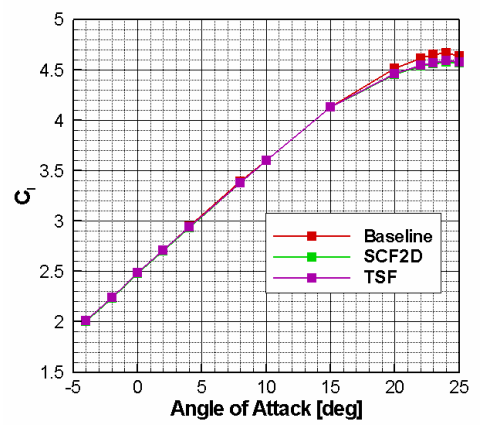

Figure 15. C_l-α curves of the baseline, SCF2D, and TSF (2D simulation using UPACS-1.4)

Based on the 2D airfoil section design, experiment was performed [24]. The results were successful for the SCF2D case, which meant that the aerodynamic performance is maintained and noise is reduced, simultaneously. On the other hand, noise reduction property of TSF was not as good as predicted from 2D CFD, although its aerodynamic performance was maintained. From the experiment, local flow separation in spanwise direction was presumed. As shown in Fig. 7, spanwise distribution in C_p is observed on this model. For example, the suction peak on the main element at 20% cross section is higher than that of 80%, which means that outboard location has lower effective AoA. To evaluate the 3D effect, steady state computations are performed using TAS code. Since mesh generation is necessary for each different low noise device, rapid meshing is crucial for obtaining results promptly. In this aspect, unstructured grid solver is advantageous compared with structured grid solver. Figure 16 shows the surface mesh around the slat tip region.

Figure 17 shows Mach number distributions at two different cross sectional planes (η=20, and 80%). The flow conditions are freestream velocity of 60m/s and AoA of 8 degrees. The flow inside the slat cove for SCF2D is attached throughout the whole span, but flow separation is observed at the outboard side for TSF. The leading edge curvature of the TSF is relatively small compared with the baseline or SCF2D, which means that when AoA decreases, sudden separation will occur at the lower surface. This indicates the noise generation around this portion of the wing. Thus, follow-up experiment for TSF will be planed in the near future.

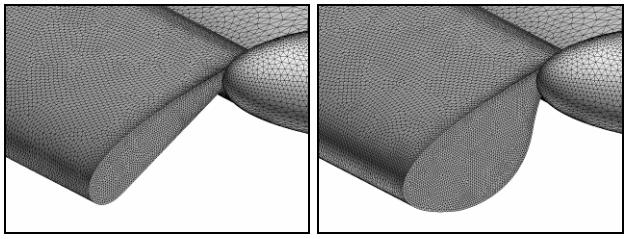

Figure 16. 3D surface grid for each low noise slat

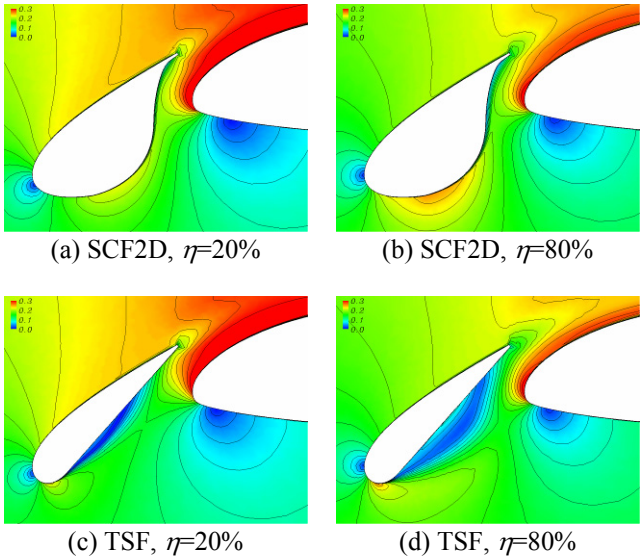

(a) SCF2D, η=20% (b) SCF2D, η=80%

(c) TSF, η=20% (d) TSF, η=80%

Figure 17. Mach number distribution around baseline, SCF2D, and TSF at η=20 and 80% spanwise location (3D simulation using TAS)

5 Conclusions.

Overview of the computational fluid dynamics (CFD) research activities, associated with a simplified high-lift-device wind tunnel model (OTOMO) was described. Three different CFD codes were used to investigate the flow around the OTOMO focusing on different aspects. First, two different codes, UPACS (structured grid) and TAS (unstructured

grid), were used to estimate the aerodynamic performance. Secondly, unsteady flow simulation was performed to understand the noise generation mechanism around OTOMO, specially, slat noise. For this purpose, UPACS-LES code was used. Validation of the computational results was performed through comparison with the experimental results. The noise reduction devices were designed based on the CFD and were tested in the wind tunnel. The SCF design was successful but TS needs further improvement for further noise reduction. The causes of unexpected results were investigated by CFD results. Thus, follow-up experiment will be planed in the near future. All of the computations were performed parallel to the wind tunnel experiments, which made the overall program successful.

References

[1] Astley, J., Predicting and Treating Fan and Turbomachinery Noise Current Technology, Research & Facilities, UK-Japan Bilateral Workshop (Aircraft Emissions and Noise), Tokyo, 2006.

[2] Hardin, J. C., Airframe self-noise: Four years of research; aircraft noise reduction for commercial aircraft, NASA-TM-X-73908, 1976.

[3] Yokokawa, Y., Murayama, M., Ito, T., and Yamamoto, K., Experiment and CFD of a High-Lift Configuration Civil Transport Aircraft Model, AIAA paper 2006-3452, 2006.

[4] Ito, T., Yokokawa, Y., Ura, H., Kato, H., Mitsuo, K., and Yamamoto, K., High-Lift Device Testing in JAXA 6.5M X 5.5M Low-Speed Wind Tunnel, AIAA Paper 2006-3643, 2006.

[5] Ura, H., Yokokawa, Y., and Ito, T., Phased Array Measurement of High Lift Devices in Low Speed Wind Tunnel, AIAA paper 2006-2565, 2006.

[6] Yokokawa, Y., Imamura, T., Ura, H., Uchida, H., Ito, T., and Yamamoto, K., Studies on Airframe Noise Generation at High-lift Devices in Relation to Aerodynamic Performances, AIAA-2008-2960, 2008

[7] Ura, H., Yokokawa, Y., Imamura, T., Ito T., and Yamamoto K., Investigation of Airframe Noise from High Lift Configuration Model, AIAA Paper 2008-19, 2008.

[8] Yamane, T., Yamamoto, K., Enomoto, S., Yamazaki, H., Takaki, R., and Iwamiya, T., Development of a Common CFD Platform - UPACS -, in Parallel Computational Fluid Dynamics - Proceedings of the Parallel CFD 2000 Conference, Trondheim, Norway, Elsevier Science B. V., 2001, 257-264.

[9] Takaki, R., Yamamoto, K., Yamane, T., Enomoto, S., and Mukai, J., The Development of the UPACS CFD Environment, in High Performance Computing Proceedings of 5th International Sympoium, ISHPC 2003, Ed. Veidenbaum et al., Springer, 2003, pp307-319.

[10] Murayama, M., Yamamoto, K., and Kobayashi, K., Validation of Flows on High-Lift Configurations by Structured- and Unstructured- Mesh Method, AIAA paper 2005-1226, 43rd AIAA Aerospace Sciences Meeting and Exhibit

[11] Nakahashi, K., Togashi, F., Fujita, T., and Ito, Y., Numerical Simulations on Separation of Scaled Supersonic Experimental Airplane from Rocket Booster at Supersonic Speed, AIAA Paper 2002-2843, June 2002.

[12] Murayama, M., Togashi, F., Nakahashi, K., Matsushima, K., and Kato, T. Simulation of Aircraft Response to Control Surface Deflection Using Unstructured Dynamic Grids, Journal of Aircraft, Vol. 42, No. 2, March-April 2005, pp. 340-346.

[13] Murayama, M. and Yamamoto, K., Comparison Study of Drag Prediction for the 3rd CFD Drag Prediction Workshop by Structured and Unstructured Mesh Method, AIAA Paper 2007-0258, Jan. 2007.

[14] Ito, Y., Shih, A. M., Soni, B. K. and Nakahashi, K., Multiple Marching Direction Approach to Generate High Quality Hybrid Meshes, AIAA Journal, Vol. 45, No. 1, January 2007, pp. 162-167

[15] Ito, Y., Shih, A. M. and Soni, B. K., Octree-Based Unstructured Hexahedral Mesh Generation, 3rd Asian-Pacific Congress on Computational Mechanics (APCOM'07) in conjunction with 11th International Conference on the Enhancement and Promotion of Computational Methods in Engineering and Science (EPMESC XI), Kyoto, Japan, December 2007

[16] Ito, Y., Shih, A. M. and Soni, B. K., Reliable Isotropic Tetrahedral Mesh Generation Based on an Advancing Front Method, Proceedings of the 13th International Meshing Roundtable, Williamsburg, VA, September 2004, pp. 95-105

[17] Ito, Y., Murayama, M., Yamamoto, K., Shih, A. M. and Soni, B. K., Efficient CFD Evaluation of Small Device Locations with Automatic Local Remeshing, AIAA Paper 2008-7180, 26th AIAA Applied Aerodynamics Conference, Honolulu, Hawaii, August 2008, accepted.

[18] Imamura, T., Enomoto, S., Yokokawa, Y., and Yamamoto, K., Three-Dimensional Unsteady Flow Computations Around a Conventional Slat of High-Lift Devices, AIAA Journal, 2008, vol.46, no.5, pp.1045-1053

[19] Imamura, T., Enomoto, S., and Yamamoto K., Noise Generation around NACA0012 Wingtip using Large-Eddy-Simulation, 25th Congress of the International Council of the Aeronautical Sciences (ICAS) Hamburg, Germany, 2006.

[20] Enomoto, S, Nozaki, O., Imamura, T., and Yamamoto, K., Large-Eddy Simulation of Jet Noise using Multi-block Structured Grid, IGTC07 ABS-148, International Gas Turbine Congress 2007, Tokyo, 2007.

[21] Kobayashi, M. H. On a Class of Pade Finite Volume Methods, Journal of Computational Physics, Vol.156, No.1, November 1999, pp137-180.

[22] Murayama, M., Yokokawa, Y. and Yamamoto, K., CFD Validation Study for a High-Lift Configuration of a Civil Aircraft Model, AIAA-2007-3924, 2007

[23] Kuroda, M., Yokokawa, Y., Murayama, M., Nakahashi, K. and Fukunishi, Y., Flap-Edge Flowfield and Noise in Civil Transport Aircraft Model, AIAA-2007-224 45th AIAA Aerospace Sciences Meeting and Exhibit, Reno, Nevada, Jan. 8-11, 2007

[24] Imamura, T., Ura, H., and Yokokawa, Y., Hirai, T., and Yamamoto, K., Numerical and Experimental Research of Low-Noise Slat Using Simplified High-lift Model, AIAA-2008-2918, 2008

Copyright Statement